Preprint Title	A polar mineral tourmaline enables synthesis of 0D/2D CuO photocatalyst with enhanced photocatalytic activity
Authors	Changqiang Yu, Min Wen, Zhen Tong, Shuhua Li, Yanhong Yin, Xianbin Liu, Yesheng Li, Tongxiang Liang, Ziping Wu and Dionysios D. Dionysiou
Publication Date	03 Jan 2020
Article Type	Full Research Paper
Supporting Information File 1	Supporting+Information(1).docx; 378.8 KB
ORCID® iDs	Yanhong Yin - https://orcid.org/0000-0002-5531-5582; Dionysios D. Dionysiou - https://orcid.org/0000-0002-6974-9197

A polar mineral tourmaline enables synthesis of 0D/2D CuO photocatalyst with enhanced photocatalytic activity

Changqiang Yu[1], Min Wen[1], Zhen Tong[1], Shuhua Li[1], Yanhong Yin[*,1,2,3], Xianbin Liu[1], Yesheng Li[1], Tongxiang Liang[1], Ziping Wu[1] and Dionysios D. Dionysiou[*,2]

[1] School of Materials Science and Engineering, Jiangxi University of Science and Technology, Ganzhou 341000, China

[2] Environmental Engineering and Science Program, Department of Chemical and Environmental Engineering, University of Cincinnati, Cincinnati, OH 45221, United States

[3] Chongyi Zhangyuan Tungsten Co., Ltd., Ganzhou 341000, China

*Corresponding authors. E-mail: yinyanhong@jxust.edu.cn (Y. H. Yin), dionysios.d.dionysiou@uc.edu (D. D. Dionysiou).

Abstract

Photocatalysis is considered to be a green and promising technology for transforming organic contaminants into nontoxic products. In this work, the CuO/tourmaline composite with zero-dimensional/two-dimensional (0D/2D) CuO architecture was obtained via a facile hydrothermal process. CuO chemically interacted with tourmaline via Si-O-Cu bond. The specific surface area of the CuO/tourmaline composite (23.60 m^2 g^{-1}) was larger than that of pristine CuO (3.41 m^2 g^{-1}). Three predominant reactive species of superoxide radical ($O_2^{\bullet-}$), hydroxyl radical (•OH), and h^+ were generated by the CuO/tourmaline composite aqueous suspension system under light irradiation. The CuO/tourmaline composite exhibited excellent photocatalytic capacity for the decomposition of organic pollutants, which was ascribed to the increase in the quantity of adsorption-photoreactive sites and the efficient utilization of photoinduced charge carriers benefited from tourmaline. This study offered a facile strategy for the construction of 0D/2D CuO structure and the design of tourmaline-based functional composite photocatalysts for the treatment of organic contaminants in waster.

Keywords: Photoinduced charge separation; Photocatalytic activity; 0D/2D CuO; Specific surface area; Tourmaline

Introduction

Developing a novel semiconductor with excellent photoreactive activity toward the treatment of organic contaminants in wastewater is in urgent need owing to the deterioration of the ecological environment [1]. Metal oxides, such as ZnO [2], TiO_2 [3], Fe_2O_3 [4], and CuO [5], have been demonstrated to be promising photocatalysts. In particular, the band gap energy (E_g) of the p-type CuO semiconductor is ~1.2 eV [6]. The application of CuO covered the field of the photocatalytic degradation of organic contaminants [7], photocatalytic reduction of CO_2 [8, 9], photocatalytic splitting of water [10], etc. The nanoscale CuO has been widely studied owing to its increased surface defects and higher specific surface area compared with the bulk one [11, 12]. However, the agglomeration of the nanoscale CuO resulted from the high surface energy and the quick recombination of the photoinduced charge carriers restricted the photocatalytic activity [13, 14]. At present, the construction of CuO-based heterostructures (e.g., 0D/2D CuO/TiO_2, 0D/3D CuO/ZnO, 2D/2D CuO/Fe_2O_3, 0D/2D CuO/C_3N_4, 2D/0D CuO/Ag_3PO_4) [6, 12, 15-17] and the dispersion of CuO on supporting materials (e.g., graphene, carbon nanotube) [7, 18] are considered to be the effective ways to address these problems. However, it is difficult to obtain the uniform heterostructures, and the preparation process is either complex or of high cost. Therefore, exploring a low-cost and easily-synthesized CuO-based materials with good photoreactive properties is still an urgent task.

Tourmaline is a type of natural polar mineral, and its general formula could be written as $XY_3Z_6(T_6O_{18})(BO_3)_3V_3W$, where X: K^+ ,Na^+, Ca^{2+}, □ (vacancy); Y: Li^+, Fe^{2+}, Mn^{2+}, Mg^{2+}, Fe^{3+}, Al^{3+}, Cr^{3+}, V^{3+}, Ti^{4+}; Z: Fe^{3+}, Al^{3+}, Cr^{3+}, V^{3+}; T: Al^{3+},

B^{3+}, Si^{4+}; *B*: B^{3+}; *V*: OH^-, O^{2-}; *W*: OH^-, F^-, O^{2-} [19]. The spontaneous permanent polarization provided tourmaline with the generation of 10^6-10^7 V m^{-1} electronic field on its surface [20]. The electronic field could boost the separation of the photoinduced charge carriers [2, 21, 22]. Furthermore, tourmaline could augment the oxygen dissolved into water due to its infrared radiation effect [22, 23], which contributed to accelerate the photocatalytic oxidation reactions. Tourmaline is a promising functional mineral material for accepting the photogenerated e^- due to its special electric field.

Herein, we reported a successful synthesis of the CuO/tourmaline composite photocatalyst with 0D/2D CuO geometric structure by a facile precipitation-hydrothermal process. This work firstly highlighted a simple way to promote the photocatalytic activity of CuO by coupling with the polar mineral tourmaline, and provided an ideal example for developing the easily-synthesized and low-cost tourmaline-based photocatalysts. The morphology, microstructure, pore structure, optical properties, and durability of the samples were characterized and discussed. The photocatalytic degradation performance of the CuO/tourmaline composite was investigated, and a plausible mechanism was proposed.

Experimental

Materials

The tourmaline sample used in this study was obtained from Hebei province, China. It was crushed and purified through a hand-selecting process. Then, distilled water was used to rinse the tourmaline sample, and the obtained sample was dried at 110 ℃. Finally, the obtained sample was ground by a planetary mill and sized (325 mesh) for use in the experiments.

Cupric acetate monohydrate ($Cu(CH_3COO)_2 \cdot H_2O$, AR), sodium hydroxide

(NaOH, AR), sodium sulfite (Na_2SO_3, AR), sodium sulfide (Na_2S, AR), 5, 5-dimethyl-1-pyrroline N-oxide (DMPO, AR), disodium ethylenediaminetetraacetate (EDTA, AR), tert-butyl alcohol (TBA, AR), 1,4-benzoquinone (BQ, AR), and Nafion were purchased from Aladdin Chemistry Co., Ltd., China.

Synthesis of the photocatalysts

Hydrothermal process was employed to synthesize the CuO/tourmaline composite. In detail, 0.50 g of tourmaline powders and 40 mL of distilled water were added into a beaker followed by 20 min of magnetic stirring, and the obtained suspension was sonicated for 20 min to ensure the formation of the homogeneous suspension A. Then, 1.25 g of $Cu(CH_3COO)_2{\cdot}H_2O$ was dissolved into suspension A with the formation of suspension B. The homogeneous solution C was obtained by dissolving 0.50 g of NaOH into 20 mL of distilled water, and it was dropwise mixed with suspension B with vigorous stirring for 30 min. Finally, the as-formed suspension was transferred into a polytetrafluoroethylene reactor with the total volume of 100 mL and kept at 180 ℃ for 6 h. After naturally cooled down, deionized water was used to wash the resultant products and obtained samples were dried under 70 ℃, named as CuO/tourmaline-1:1 (1:1 in mass ratio of the CuO:tourmaline). By controlling the dosage of $Cu(CH_3COO)_2{\cdot}H_2O$ and NaOH in proportion to acquire the CuO/tourmaline composites in different mass ratios of the CuO:tourmaline.

Characterization

X-ray diffraction (XRD) patterns were obtained step scan mode performed with a DX-2700 diffractometer (Dandong Haoyuan Instrument Co. Ltd., China) with Ni-filtered Cu Kα radiation (λ=0.1.541 Å), 10-80° 2θ scan. X-ray

photoelectron spectra (XPS) were recorded using a K-ALPHA instrument (ThermoFisher Scientific, USA). A MIRA3 field emission scanning electron microscope (SEM, Tescan, Czech) was used to observe the geometry morphology. A Titan G2 60-300 transmission electron microscope (TEM, FEI, USA) was employed to analyze the microstructure. A NEXUS 670 spectrometer (Thermo Nicolet, USA) was employed for recording the Fourier transform infrared (FTIR) spectra. UV-visible diffuse reflectance spectra were measured using a Lambda 750S UV-vis spectrophotometer (Perkin-Elmer, USA). Photoluminescence (PL) spectra were measured with a F-4600 fluorescence spectrophotometer (Hitachi, Japan). Transient photocurrent was measured with two Interface 1010E electrochemical workstations (Gamry, USA) using Na_2SO_3 (0.2 M) and Na_2S (0.2 M) solutions with the volume ratio of 1:1 as electrolyte under LED lamp (λ=470 nm) irradiation. Electron paramagnetic resonance (EPR) spectra were analyzed using an A300 spectrometer (Bruker, Germany) with DMPO as free radical scavenger. Surface properties was characterized via an ASAP 2020 instrument (Micromeritics, USA). Zeta potential was measured with a ZETASIZER NANO ZS90 instrument (Malvern, UK).

Photocatalytic activity evaluation

The performance was examined by degradation of methylene blue (MB) with light irradiation simulated by a 300 W Xe lamp with an UV cut-off filter. In detail, 0.05 g of the as-synthesized photocatalyst was added into 100 mL of 0.01 g L^{-1} methylene blue (MB) aqueous solution, followed by 1 h of magnetic stirring in the dark to make sure the adsorption saturation of MB onto the photocatalysts has been achieved. Then, the photocatalyst-dye aqueous suspension system was exposed to light. 4 mL of the aqueous suspension was extracted every 20 min and clarified by centrifugation for the

measurement of absorbance, which can monitor the progress of the photocatalytic degradation reactions. For the durability test, the used photocatalyst was firstly rinsed with ethanol and deionized water by centrifugation, then it was gathered by using MB aqueous for the subsequent experiments.

Results and Discussion

Figure 1a displayed the XRD spectra of the samples. The main peaks with the 2θ values of 32.51°, 35.54°, 38.71°, 48.72°, 53.49°, 58.26°, 61.52°, 66.22°, 68.12°, 72.37°, and 75.24° matched well with those of the monoclinic CuO (JCPDS 48-1548). As for tourmaline, the main diffraction peaks with the 2θ values of 13.92°, 17.82°, 19.24°, 21.02°, 22.25°, 25.68°, 29.57°, 30.23°, 34.74°, 37.86°, 38.32°, 41.21°, 41.64°, 42.62°, 44.35°, 47.32°, 48.59°, 55.38°, 55.85°, 57.69°, 61.69°, 64.06°, and 74.56° were assigned to the (101), (021), (300), (211), (220), (012), (410), (122), (051), (232), (511), (502), (431), (303), (152), (342), (143), (063), (271), (550), (054), (713), and (505) planes of schorl (JCPDS 85-1811). There was not peak of impurity being detected, indicating the predominance of CuO and tourmaline in the composite.

Surface element component and valence state of the as-synthesized photocatalysts were investigated with XPS (Figure 1b). Two XPS peaks with the binding energies of 932.93 eV and 952.79 eV corresponded to $Cu2p_{3/2}$ and $Cu2p_{1/2}$, respectively. The satellite peaks with the higher binding energies of 941.78 eV and 961.45 eV were observed [24]. In comparison to the pure CuO, the binding energies of $Cu2p_{3/2}$ and $Cu2p_{1/2}$ for the CuO/tourmaline composite shifted to 933.49 eV and 953.37 eV, respectively, providing an evidence for the chemical interaction between CuO and tourmaline.

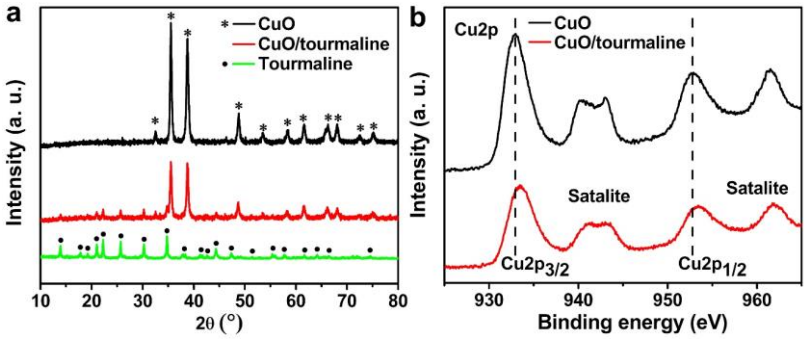

166

167 **Figure 1:** (a) XRD spectra of the CuO, tourmaline, and CuO/tourmaline

168 composite. (b) High-resolution Cu2p XPS of the CuO and CuO/tourmaline

169 composite.

170

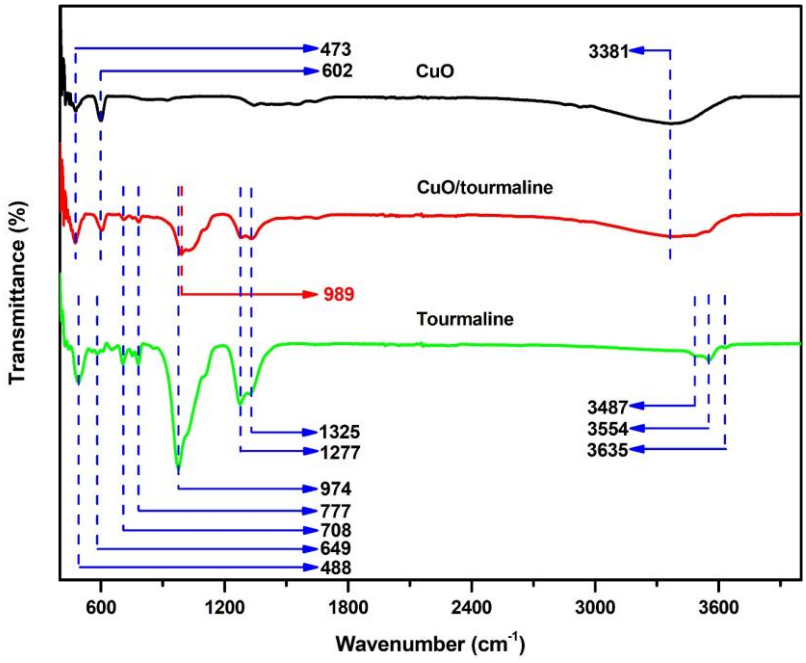

171

172 **Figure 2:** FTIR spectra of the CuO, tourmaline, and CuO/tourmaline

173 composite.

174

175 It is convenient to detect the chemical bonds in complex materials by FTIR spectra.

176 As shown in Figure 2, the three bands appeared at 3487 cm^{-1}, 3554 cm^{-1}, and 3635 cm^{-1}

177 resulted from the vibration of the three OH groups in tourmaline [2]. The bending

178 vibration of the Si-O group were detected at 488 cm^{-1} [25]. The band of 649 cm^{-1} was

179 due to the R^{IV}-O (R=Al, Fe, Mg, Mn) stretching vibration, and the wavenumbers of 708

cm^{-1} and 777 cm^{-1} came from the Si-O-Si stretching vibration [2, 26]. A well-resolved band at 974 cm^{-1} originated from the Si-O stretching vibration [27], and it shifted to 989 cm^{-1} with a blue-shift of 15 cm^{-1} for the CuO/tourmaline composite compared with that of the pristine tourmaline. The result indicated that tourmaline could chemically interact with CuO via Si-O-Cu bond. The two bands at 1277 cm^{-1} and 1325 cm^{-1} came from the planar three-fold boron stretching vibration. As for CuO, the wavenumbers of 473 cm^{-1} and 602 cm^{-1} resulted from the vibration of the Cu-O group [28]. In addition, the O-H stretching vibration band of the absorbed water appeared at 3381 cm^{-1} [29].

SEM and TEM were carried out to characterized the morphology and microstructure of the samples. Tourmaline displayed a granular morphology with the size of 0.1-1.0 μm (Figure 3a and d). The pure CuO was composed of highly stacked smooth 2D nanoflakes with the thickness of ~50 nm (Figure 3b and e). With the addition of tourmaline, plenty of 0D CuO nanoparticles (~20 nm) generated on the surface of 2D CuO nanoflakes (Figure 3c and f). The 0D CuO nanoparticles roughened the surface of 2D CuO nanoflakes, and significantly alleviated the agglomeration of 2D CuO nanoflakes. The lattice fringes with the *d* spacing of 0.34 nm and 0.25 nm matched well with the (012) plane of tourmaline and the (002) plane of CuO, respectively (Figure 3d-e, inset). There was intimate interfacial contact between CuO and tourmaline (Figure 3f, inset), which provided channels for the fast transfer of photoinduced e^- from the conduction band (CB) of CuO to tourmaline. The energy dispersive X-ray (EDX) elemental mapping verified the uniform dispersion of CuO throughout the CuO/tourmaline composite (Figure 3g).

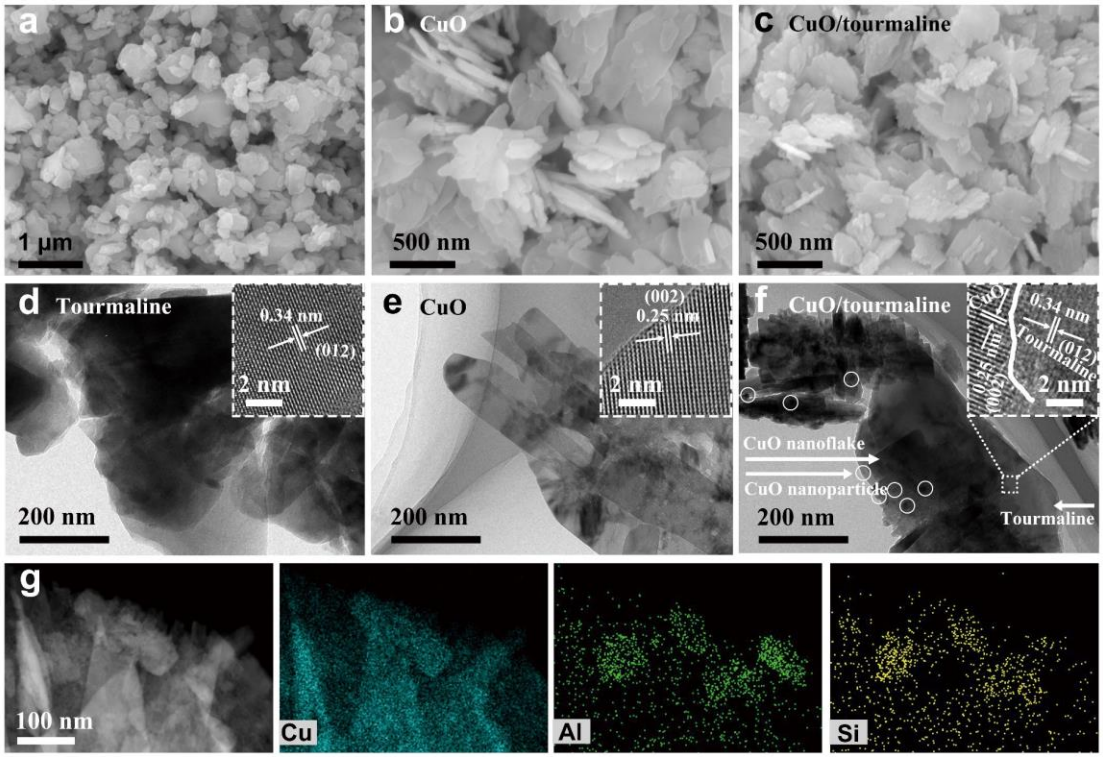

Figure 3: SEM images of (a) tourmaline, (b) CuO, and (c) CuO/tourmaline composite. TEM images of (d) tourmaline, (e) CuO, and (f) CuO/tourmaline composite, the insets showed the corresponding high-resolution TEM images. (g) EDX element mapping images of Cu, Al, and Si for the CuO/tourmaline composite.

The pore structure of the photocatalysts were analyzed by the nitrogen adsorption-desorption isotherms. As shown in Figure 4a, CuO, tourmaline, and CuO/tourmaline composite exhibited type-IV adsorption isotherms, which were the characteristics of mesoporous materials. The Brunauer–Emmett–Teller (BET) specific surface area of the CuO/tourmaline composite with 0D/2D CuO structure (23.60 $m^2 g^{-1}$) was larger than those of CuO (3.41 $m^2 g^{-1}$) and tourmaline (12.78 $m^2 g^{-1}$). Meanwhile, the total pore volume and pore size of the CuO/tourmaline composite (13.744 nm, 0.081 $cm^3 g^{-1}$), CuO (21.960 nm, 0.019 $cm^3 g^{-1}$), and tourmaline (15.219 nm, 0.049 $cm^3 g^{-1}$) were analyzed according to the Barrett–Joyner–Halenda (BJH) method (Figure 4b). The enlarged pore

volume and BET specific surface area confirmed that the CuO/tourmaline composite with 0D/2D CuO structure possessed increased number of active sites.

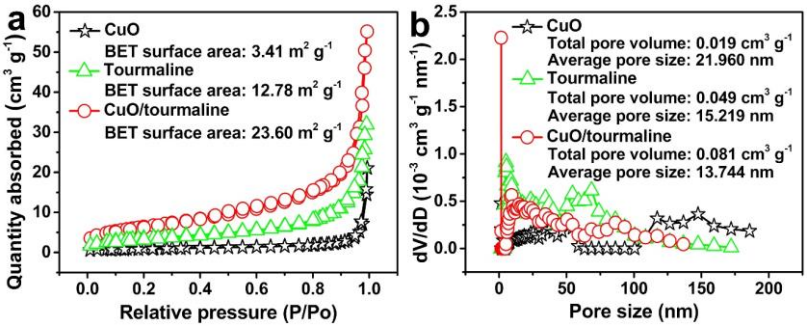

Figure 4: (a) Nitrogen adsorption-desorption isotherms and (b) BJH pore size distribution of the CuO, tourmaline, and CuO/tourmaline composite.

UV-vis diffuse reflectance spectra were carried out to study the optical properties of the samples. As shown in Figure 5a, the CuO/tourmaline composite exhibited higher optical adsorption than that of pure CuO, which was benefited from the plasmon of tourmaline units [22]. The *E*g of CuO and CuO/tourmaline composite were calculated to be 1.42 eV and 1.31 eV, respectively (Figure 5b). The decrease in *E*g of the CuO/tourmaline composite suggested a higher utilization efficiency of light [30].

Various measurements were employed to investigate the effect of tourmaline on the separation of photoinduced charge carriers. The transient photocurrent density of the CuO/tourmaline composite was higher than that of pristine CuO during the repeated switching on and off of light irradiation (Figure 5c), implying that tourmaline could facilitate the transfer of photoinduced e^-, which was also confirmed by the PL spectra (Supporting Information File 1, Figure S1). The time-resolved PL spectra revealed that the average fluorescence lifetime of the CuO/tourmaline composite (2.94 ns) was shortened with reference

to pristine CuO (3.24 ns) (Figure 5d), which could be ascribed to the improvement of the nonradiative decay pathway in the composite [31]. The above analyses confirmed the role of tourmaline in suppressing the recombination of photoinduced charge carriers.

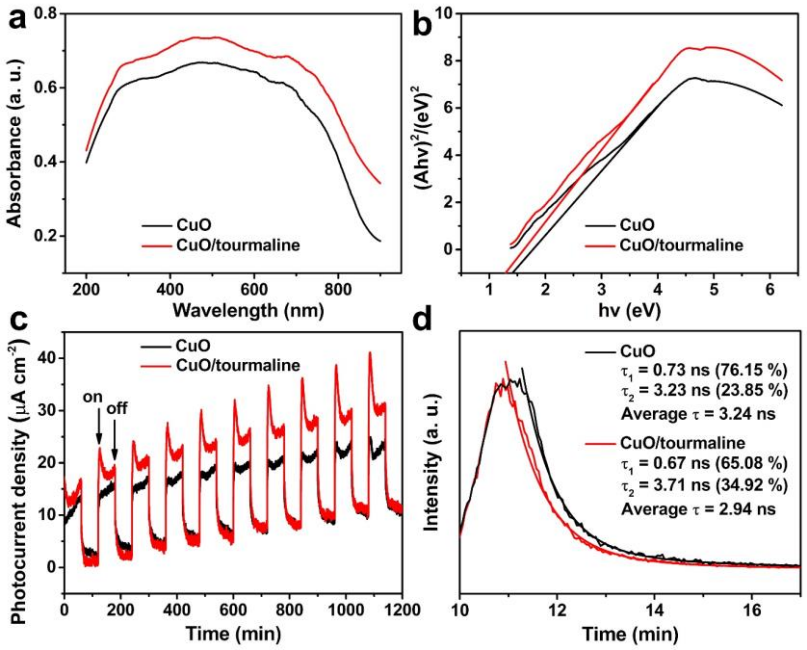

Figure 5: (a) UV-vis diffuse reflectance spectra, (b) plots of $(Ahv)^2$ vs. hv, (c) transient photocurrent, and (d) time-resolved PL spectra of the CuO and CuO/tourmaline composite.

The photocatalytic degradation of MB was conducted to evaluate the properties of the samples. The CuO/tourmaline-4:1 composite exhibited the optimum activity with MB degradation (%) of 99.6 % within 140 min (Figure 6a). The apparent pseudo-first-order equation was adopted to interprete the photocatalytic degradation kinetics. The corresponding fitted lines of -ln (C/Co) vs. time are exhibited in Figure 6b. The *k* value of the CuO/tourmaline-4:1 composite was larger than that of the other composites and was three times higher than that of CuO (Figure 6c), which proved that the CuO/tourmaline composite

was successfully prepared and showed higher photocatalytic organic oxidation ability.

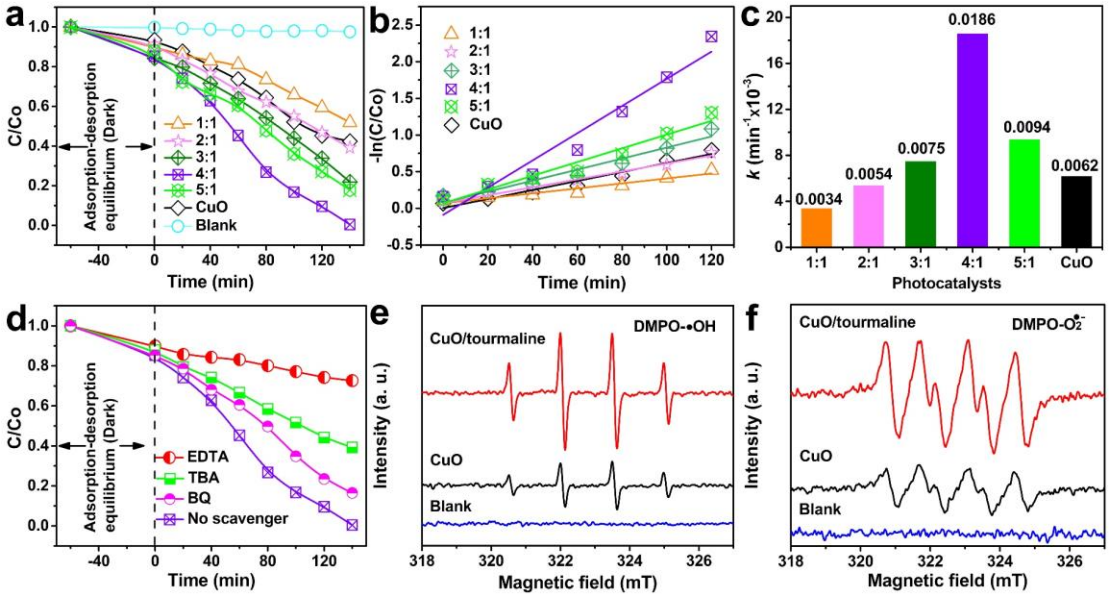

Figure 6: (a) MB degradation, (b) the apparent pseudo-first-order kinetic plots, and (c) rate constant *k* of the CuO/tourmaline composite in different mass ratios of the CuO:tourmaline. (d) Photocatalytic degradation curves of MB over the CuO:tourmaline-4:1 composite with different reactive species scavengers. Experimental conditions: $[MB]_0$ = 0.01 g L^{-1}, $[photocatalyst]_0$ = 0.5 g L^{-1}, volume = 100 mL, temperature = 25 ℃. EPR signals of (c) DMPO-•OH and (d) DMPO-$O_2^{\bullet-}$ adducts of the CuO and CuO/tourmaline composite under visible light irradiation for 20 min.

Trapping experiments were carried out to verify the predominant reactive species participated in the photocatalytic organic oxidation reactions. •OH, $O_2^{\bullet-}$, and h^+ were trapped by TBA, BQ, and EDTA, respectively [32, 33]. Judging from Figure 6d, the addition of TBA, BQ, and EDTA resulted in decrease in MB degradation (%) from 99.6 % to 60.8 %, 83.5 %, and 27.4 %, respectively. The results revealed that h^+, •OH, and $O_2^{\bullet-}$ involved in the photocatalytic reactions,

and h^+ contributed to higher organic oxidation than •OH and $O_2^{\bullet-}$. EPR measurement was used to directly probe the generation of reactive species in the CuO/tourmaline composite aqueous suspensions by using DMPO as trapping agent. As shown in Figure 6e and f, no EPR signals were observed in the absence of light irradiation. When exposed to light irradiation, the intensity of both DMPO-$O_2^{\bullet-}$ and DMPO-•OH adducts for the CuO/tourmaline composite were stronger than those of pure CuO. The results clearly verified that the CuO/tourmaline composite could produce higher level of reactive species than pure CuO. The more reactive species the composite produced, the higher photocatalytic activity the composite exhibited.

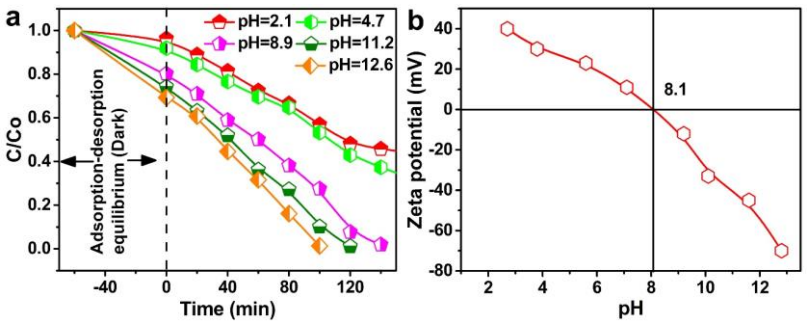

Figure 7: (a) MB degradation over the CuO/tourmaline-4:1 composite with different initial solution pH. Experimental conditions: $[MB]_0$ = 0.01 g L^{-1}, $[photocatalyst]_0$ = 0.5 g L^{-1}, volume = 100 mL, temperature = 25 ℃. (b) Zeta potential of the CuO/tourmaline composite under various pH.

The photocatalytic performance of the CuO/tourmaline composite was also tested under different conditions. The composite with the synthesis temperature of 180 °C exhibited optimum photocatalytic activity (Supporting Information File 1, Figure S2), implying that the synthesis temperature of 180 °C could optimize 0D/2D CuO structure and interfacial interaction between CuO and

tourmaline. The initial solution pH affected the photocatalytic performance mainly via changing the adsorption of dyes onto photocatalysts (Figure 7a), as adsorption occurred firstly during the photodegradation reactions [34]. The isoelectric point of the CuO/tourmaline composite was determined to be 8.1 (Figure 7b). When the pH value of the solution was less than 8.1, the adsorption between the positively charged composite and the positively charged MB was weakened by electrostatic repulsion. When the pH value of the solution was larger than 8.1, the adsorption between the negatively charged composite and the positively charged MB was strengthened by electrostatic attraction.

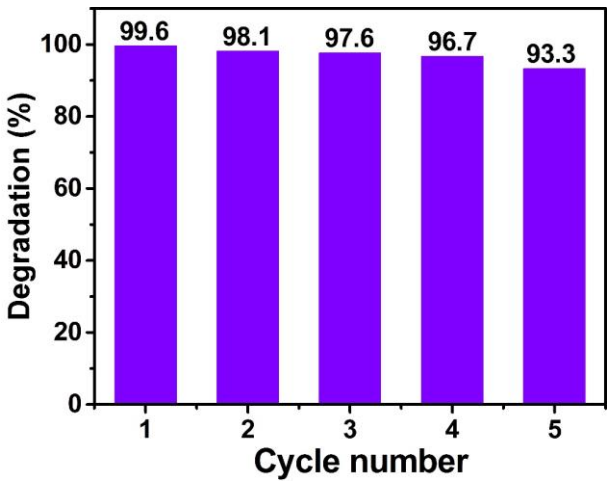

Figure 8: Five successive photocatalytic MB degradation (%) over the CuO/tourmaline-4:1 composite. Experimental conditions: $[MB]_0$ = 0.01 g L^{-1}, $[photocatalyst]_0$ = 0.5 g L^{-1}, volume = 100 mL, temperature = 25 ℃.

The durability and stability of the CuO/tourmaline composite were evaluated by five successive photocatalytic degradation tests. As shown in Figure 8, MB degradation (%) over the CuO/tourmaline composite remained 93.3 % after being used for five times. There was not obvious distinction between the XRD patterns and FTIR spectra of the fresh and reused CuO/tourmaline

composite, except for a slight decrease in the intensity (Supporting Information File 1, Figure S3). The results implied that the as-synthesized CuO/tourmaline composite was durable and stable toward the photocatalytic decomposition of organic pollutants, which might be because tourmaline protected CuO from photocorrosion by facilitating the fast transfer of photogenerated e^-.

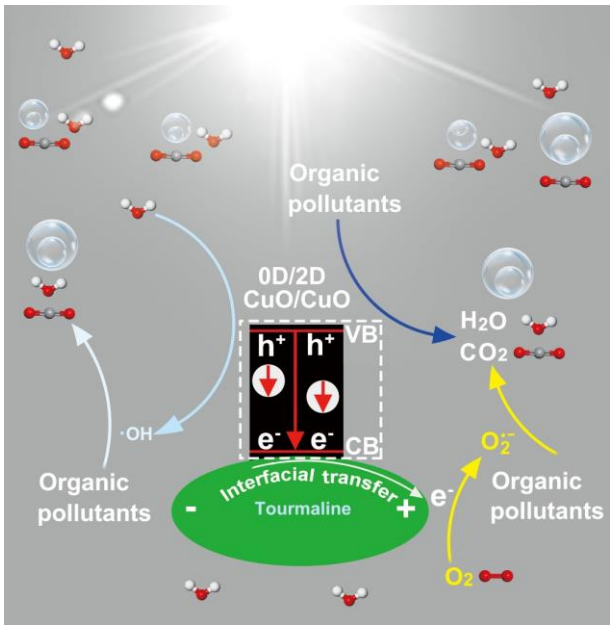

Figure 9: Schematic illustration of the role of tourmaline in enhancing the photocatalytic activity of CuO.

With a combination of the analyses carried out above, a plausible mechanism for strengthening the photocatalytic degradation activity of CuO with tourmaline was proposed and shown in Figure 9. The e^- in the valence band (VB) of CuO was excited with the generation of e^-/h^+ pairs under light irradiation (Equation 1). Tourmaline facilitate the transfer of photoinduced e^- via its strong electronic field (Equation 2). The separated e^- reacted with the oxygen dissolved into water with the formation of $O_2^{\bullet-}$ (Equation 3). Meanwhile, a portion of h^+ reacted with water to generate •OH (Equation 4). Reactive species of h^+, •OH,

and $O_2^{\bullet-}$ synergistically participated in the organic oxidation reactions (Equation 5). The exposure of more adsorption-photoreactive sites and the efficient utilization of photoinduced e^-/h^+ pairs enabled by tourmaline contributed to the enhanced photocatalytic activity.

$$CuO + hv \rightarrow CuO\ (e^-_{CB}) + CuO\ (h^+_{VB}) \quad (1)$$

$$CuO\ (e^-_{CB}) + \text{tourmaline} \rightarrow CuO + \text{tourmaline}\ (e^-) \quad (2)$$

$$\text{tourmaline}\ (e^-) + O_2 \rightarrow O_2^{\bullet-} + \text{tourmaline} \quad (3)$$

$$CuO\ (h^+_{VB}) + H_2O \rightarrow \bullet OH + H^+ + CuO \quad (4)$$

$$h^+, \bullet OH, O_2^{\bullet-} + \text{absorbed organic pollutants} \rightarrow \text{intermediates} \rightarrow CO_2, H_2O \quad (5)$$

Conclusions

To sum up, the CuO/tourmaline composite with 0D/2D CuO architecture was successfully obtained by using a facile hydrothermal process. The CuO/tourmaline composite exhibited superior photocatalytic activity toward organic oxidation, which could be ascribed to the fact that tourmaline can simultaneously enable the formation of 0D/2D CuO to increase the quantity of adsorption-photoreactive sites and promote the effective utilization of photogenerated e^-/h^+ pairs. The present study offered a facile strategy for the construction of 0D/2D CuO structure and the design of tourmaline-based functional composite photocatalysts for the oxidation of organic pollutants.

Supporting Information

Supporting Information File 1

Additional experimental data.

Acknowledgements

This work was supported by the China Scholarship Council (201908360233). D. D. Dionysiou also acknowledges support from the University of Cincinnati through a UNESCO co-Chair Professor position on "Water Access and Sustainability" and the Herman Schneider Professorship in the College of Engineering and Applied Sciences.

References

[1] Ao, M.; Liu, K.; Tang, X.; Li, Z.; Peng, Q.; Huang, J. *Beilstein J. Nanotech*. **2019**, *10*, 1412-1422. doi: 10.3762/bjnano.10.139.

[2] Yu, C.; Tong, Z.; Li, S.; Yin, Y. *Mater. Lett*. **2019**, *240*, 161-164. doi: 10.1016/j.matlet.2018.12.109.

[3] Golabiewska, A.; Paszkiewicz-Gawron, M.; Sadzinska, A.; Lisowski, W.; Grabowska, E.; Zaleska-Medynska, A.; Luczak, J. *Beilstein J. Nanotech*. **2018**, *9*, 580-590. doi: 10.3762/bjnano.9.54.

[4] Helal, A.; Harraz, F. A.; Ismail, A. A.; Sami, T. M.; Ibrahim, A. *Appl. Catal. B-Environ*. **2019**, *213*, 18-27. doi: 10.1016/j.apcatb.2017.05.009.

[5] Li, W.; He, S.; Su, Z.; Xu, W.; Wang, X. *Appl. Surf. Sci*. **2019**, *470*, 707-715. doi: 10.1016/j.apsusc.2018.11.174

[6] Alp, E.; Esgin, H.; Kazmanli, M. K.; Genc, A. *Ceram. Int*. **2019**, *45*, 9174-9178. doi: 10.1016/j.ceramint.2019.01.258.

[7] Arshad, A.; Iqbal, J.; Siddiq, M.; Ali, M. U.; Ali, A.; Shabbir, H.; Bin Nazeer, U.; Saleem, M. S. *Ceram. Int*. **2017**, *43*, 10654-10660. doi: 10.1016/j.ceramint.2017.03.165.

[8] Gusain, R.; Kumar, P.; Sharma, O. P.; Jain, S. L.; Khatri, O. P. *Appl. Catal. B-Environ*. **2016**, *181*, 352-362. doi: 10.1016/j.apcatb.2015.08.012.

[9] Li, J. Y.; Yuan, L.; Li, S. H.; Tang, Z. R.; Xu, Y. J. *J. Mater. Chem. A* **2019**, *7*,

391 8676-8689. doi: 10.1039/c8ta12427b.
392 [10] de Brito, J. F.; Tavella, F.; Genovese, C.; Ampelli, C.; Boldrin Zanoni, M. V.;
393 Centi, G.; Perathoner, S. *Appl. Catal. B-Environ.* **2018**, *224*, 136-145. doi:
394 10.1016/j.apcatb.2017.09.071.
395 [11] Long, M.; Zhang, Y.; Shu, Z.; Tang, A.; Ouyang, J.; Yang, H. *Chem. Commun*.
396 **2017**, *53*, 6255-6258. doi: 10.1039/c7cc02905e.
397 [12] Zhu, L.; Li, H.; Liu, Z.; Xia, P.; Xie, Y.; Xiong, D. *J. Phys. Chem C* **2018**,
398 *122*, 9531-9539. doi: 10.1021/acs.jpcc.8b01933.
399 [13] Malwal, D. Gopinath, P. *Catal. Sci. Technol*. **2016**, *6*, 4458-4472. doi:
400 10.1039/c6cy00128a.
401 [14] Bharathi, P.; Harish, S.; Archana, J.; Navaneethan, M.; Ponnusamy, S.;
402 Muthamizhchelvan, C.; Shimomura, M.; Hayakawa, Y. *Appl. Surf. Sci*. **2019**,
403 *484*, 884-891. doi: 10.1016/j.apsusc.2019.03.131.
404 [15] Shi, Q.; Ping, G.; Wang, X.; Xu, H.; Li, J.; Cui, J.; Abroshan, H.; Ding, H.; Li,
405 G. *J. Mater. Chem. A* **2019**, *7*, 2253-2260. doi: 10.1039/c8ta09439j.
406 [16] Duan, Y. *Mater. Res. Bull*. **2018**, *105*, 68-74. doi:
407 10.1016/j.materresbull.2018.04.038.
408 [17] Chen, J.; Liu, X. P.; Yang, X. D.; Jiang, L. L.; Mao, C. J.; Niu, H.; Jin, B. K.;
409 Zhang, S. *Mater. Lett*. **2017**, *188*, 300-303. doi: 10.1016/j.matlet.2016.10.106.
410 [18] Khusnun, N. F.; Jalil, A. A.; Triwahyono, S.; Hitam, C. N. C.; Hassan, N. S.;
411 Jamian, F.; Nabgan, W.; Abdullah, T. A. T.; Kamaruddin, M. J.; Hartanto, D.
412 *Powder Technol*. **2018**, *327*, 170-178. doi: 10.1016/j.powtec.2017.12.052.
413 [19] Song, Y.; Zhu, D.; Liang, J.; Zhang, X. *Ceram. Int*. **2018**, *44*, 15550-15556.
414 doi: 10.1016/j.ceramint.2018.05.217.
415 [20] Fu, L.; Guo, Y.; Pan, S.; Huang, J.; Wang, L. *Surf. Coat. Tech*. **2019**, *359*, 190-

196. doi: 10.1016/j.surfcoat.2018.12.020.

[21] Li, N.; Zhang, J.; Wang, C.; Sun, H. *J. Mater. Sci*. **2017**, *52*, 6937-6949. doi: 10.1007/s10853-017-0926-8.

[22] Li, K.; Chen, T.; Yan, L.; Dai, Y.; Huang, Z.; Guo, H.; Jiang, L.; Gao, X.; Xiong, J.; Song, D. *Catal. Commun*. **2012**, *28*, 196-201. doi: 10.1016/j.catcom.2012.09.008.

[23] Xue, G.; Han, C.; Liang, J.; Wang, S.; Zhao, C. *J. Nanosci. Nanotechno*. **2014**, *14*, 3943-3947. doi: 10.1166/jnn.2014.7983.

[24] Ma, P.; Yu, Y.; Xie, J.; Fu, Z. *Adv. Powder Technol*. **2017**, *28*, 2797-2804. doi: 10.1016/j.apt.2017.08.004.

[25] Makreski, P.; Jovanovski, G. *Spectrochim. Acta A* **2009**, 73, 460-467. doi: 10.1016/j.saa.2008.07.011.

[26] Zhao, C.; Liao, L.; Xia, Z.; Sun, X. *Vib. Spectrosc*. **2012**, *62*, 28-34. doi: 10.1016/j.vibspec.2012.04.010.

[27] Liu, X.; Yu, C.; Yang, W.; Xie, L.; Liang, S. *Eur. J. Mineral*. **2019**, *31*, 919-928. doi: 10.1127/ejm/2019/0031-2864.

[28] Saravanan, R.; Karthikeyan, S.; Gupta, V. K.; Sekaran, G.; Narayanan, V.; Stephen, A. *Mat. Sci. Eng. C-Mater*. **2013**, *33*, 91-98. doi: 10.1016/j.msec.2012.08.011.

[29] Umar, A.; Chauhan, M. S.; Chauhan, S.; Kumar, R.; Kumar, G.; Al-Sayari, S. A.; Hwang, S. W.; Al-Hajry, A. *J. Colloid Interf. Sci*. **2011**, *363*, 521-528. doi: 10.1016/j.jcis.2011.07.058.

[30] Shu, Z.; Zhang, Y.; Ouyang, J.; Yang, H. *Appl. Surf. Sci*. **2017**, *420*, 833-838. doi: 10.1016/j.apsusc.2017.05.219.

[31] Cao, S.; Shen, B.; Tong, T.; Fu, J.; Yu, J. *Adv. Funct. Mater*. **2018**, *28*,

1800136. doi: 10.1002/adfm.201800136.

[32] Tian, N.; Huang, H.; He, Y.; Guo, Y.; Zhang, T.; Zhang, Y. *Dalton T*. **2015**, *44*, 4297-4307. doi: 10.1039/c4dt03905j.

[33] Shi, L.; He, Z.; Liu, S. *Appl. Surf. Sci*. 2018, *457*, 30-40. doi: 10.1016/j.apsusc.2018.06.132.

[34] Tan, Y.; Yu, K.; Yang, T.; Zhang, Q.; Cong, W.; Yin, H.; Zhang, Z.; Chen, Y.; Zhu, Z. *J. Mater. Chem. C* **2014**, *2*, 5422-5430. doi: 10.1039/c4tc00423j.